

**Figure 9** Photography. [Color figure can be viewed in the online issue, which is available at [www.interscience.wiley.com](http://www.interscience.wiley.com)]

#### 4. CONCLUSIONS

Applications of DMSLR structures for band-pass filter design are presented in this article. The novel configurations of DMSLR with Hilbert-curve perturbation are constructed to improve the performance of the conventional DMSLR with T-shaped perturbation.

The performance with low insertion loss ( $-0.85$  dB), higher rejection ( $-51.82$  dB), and wider bandwidth (BW 62.3%) in cascaded DMSLR-H are presented. The frequency response of cascaded DMSLR-H can be analyzed with equivalent circuit and approximated to the Chebyshev responses with seven-order 0.5 dB ripple. The simulated results depict the identical surface current distributions according to  $TM_{110}$  configurations.

These filters can achieve a wide pass band and sharp rejection band. Its coupling way is constructed in coplanar and efficient. The structure is smaller in size and easy to fabricate. It can be applied to the microwave communication systems.

#### ACKNOWLEDGMENTS

The supports of contract NSC 96-2623-7-231-005-D are gratefully acknowledged.

#### REFERENCES

1. K. Chang and L.H. Hsieh, *Microwave ring circuits and related structures*, 2nd ed., Wiley, New Jersey, 2004.
2. I. Wolff, Microstrip bandpass filter using degenerate modes of a microstrip ring resonator, *Electron Lett* 8 (1972), 29–30.
3. J.S. Hong and M.J. Lancaster, Bandpass characteristics of new dual-mode microstrip square loop resonators, *Electron Lett* 31 (1995), 891–892.
4. H. Yabuki, M. Sagawa, M. Matsuo, and M. Makimoto, Stripline dual-mode ring resonators and their application to microwave devices, *IEEE Trans Microwave Theory Tech* 44 (1996), 723–729.
5. L. Zhu, P.M. Wecowski, and K. Wu, New planar dual-mode filter using cross-slotted patch resonator for simultaneous size and loss reduction, *IEEE Trans Microwave Theory Tech* 47 (1999), 650–654.
6. L.H. Hsieh and K. Chang, Dual-mode elliptic-function bandpass filter using one single patch resonator without coupling gaps, *Electron Lett* 36 (2000), 2022–2023.
7. M. Matsuo, H. Yabuki, and M. Makimoto, Dual-mode stepped-impedance ring resonators for bandpass filter applications, *IEEE Trans Microwave Theory Tech* 49 (2001), 1235–1240.
8. L.H. Hsieh and K. Chang, Compact, low insertion loss, sharp rejection wideband bandpass filters using dual-mode ring resonators with tuning stubs, *Electron Lett* 37 (2001), 1345–1347.
9. L.H. Hsieh and K. Chang, Dual-mode quasi-elliptic-function bandpass filter using ring resonators with enhance coupling, *IEEE Trans Microwave Theory Tech* 50 (2002), 1340–1345.
10. L.H. Hsieh and K. Chang, Compact, low insertion loss, sharp-rejection, and wide-band microstrip bandpass filters, *IEEE Trans Microwave Theory Tech* 51 (2003), 1241–1246.
11. L.H. Hsieh and K. Chang, High-efficiency piezoelectric-transducer-tuned feedback micro-strip ring-resonator oscillators operating at high resonant frequencies, *IEEE Trans Microwave Theory Tech* 51 (2003), 1141–1145.
12. B.T. Tan, S.T. Chew, M.S. Leong, and B.L. Ooi, A dual-mode band-pass filter with enhanced capacitive perturbation, *IEEE Trans Microwave Theory Tech* 51 (2003), 1906–1910.
13. A. Gorur, Realization of a dual-mode bandpass filter exhibiting either a chebyshev or an elliptic characteristic by changing perturbation's size, *IEEE Microwave Wireless Compon Lett* 14 (2004), 118–120.
14. J.S. Hong and S. Li, Theory and experiment of dual-mode microstrip triangle patch resonators and filters, *IEEE Trans Microwave Theory Tech* 52 (2004), 1237–1248.
15. L. Zhu, B.C. Tan, and S.J. Quek, Miniaturized dual-mode bandpass filter using inductively loaded cross-slotted patch resonator, *IEEE Microwave Wireless Compon Lett* 15 (2005), 22–24.
16. M.F. Lei and H. Wang, An analysis of miniaturized dual-mode band-pass filter structure using shunt-capacitive perturbation, *IEEE Trans Microwave Theory Tech* 53 (2005), 861–867.
17. X.D. Huang and C.H. Cheng, A novel coplanar-waveguide bandpass filter using a dual-mode square-ring resonator, *IEEE Microwave Wireless Compon Lett* 16 (2006), 13–15.
18. J.C. Liu, C.S. Cheng, and L. Yao, Dual-mode double-ring resonator for microstrip band-pass filter design, *Microwave Opt Technol Lett* 39 (2003), 310–314.
19. J.C. Liu, P.C. Lu, C.S. Cheng, C.H. Shie, and L. Yao, Dual-mode double-ring resonator for microstrip band-pass filter applications, *IEE Proc Microwave Antennas Propag* 151 (2004), 430–434.
20. J.C. Liu, C.Y. Wu, M.H. Chiang, and D. Soong, Improved dual-mode double ring resonator with radial stub for UWB filter design, *Microwave Opt Technol Lett* 44 (2005), 219–222.
21. T.W. Soong, J.C. Liu, C.H. Shie, and C.Y. Wu, Modified dual-mode double-ring resonators for wide band-pass filter design, *IEE Proc Microwave Antennas Propag* 152 (2005), 245–250.
22. S. Sun and L. Zhu, Wideband microstrip ring resonator bandpass filters under multiple resonances, *IEEE Trans Microwave Theory Tech* 55 (2007), 2176–2188.
23. J.C. Liu, P.C. Lu, J.M. Chang, C.H. Chien, and C.P. Kuei, Novel dual-mode square-loop resonators using Hilbert perturbation for simultaneous size reduction and mode splitting, *Microwave Opt Technol Lett* 49 (2007), 1735–1739.
24. W.H. Tu and K. Chang, Piezoelectric transducer-controlled dual-mode switchable bandpass filter, *IEEE Microwave Wireless Compon Lett* 17 (2007), 199–201.
25. H. Kuan and H.Y. Pan, Design of a dual-mode bandpass filter with wide stopband performance for GPS application, *Microwave Opt Technol Lett* 50 (2008), 445–447.
26. P. Cai, Z. Ma, X. Guan, Y. Zhang, B. Chen, and B. Xu, Dual-mode square ring resonators for design of millimeter-wave ultra-wideband bandpass filter, *Microwave Opt Technol Lett* 50 (2008), 879–883.
27. C.Y. Hung, M.H. Weng, S.B. Zhong, S. Wu, and M.S. Lee, Design of the wideband dual-mode bandpass filter using stepped impedance resonators, *Microwave Opt Technol Lett* 50 (2008), 1104–1107.
28. Zeland Software, IE3D version 10.0, Zeland Software, Fremont, CA, 2005.

© 2009 Wiley Periodicals, Inc.

## PARALLEL IMPLEMENTATION OF THE ADI-FDTD METHOD

T. Stefański and T. D. Drysdale

Electronics Design Centre, Department of Electronics and Electrical Engineering, University of Glasgow Rankine Building, Oakfield Avenue, Glasgow G12 8LT, United Kingdom; Corresponding author: [stafan@elec.gla.ac.uk](mailto:stafan@elec.gla.ac.uk) or [t.drysdale@elec.gla.ac.uk](mailto:t.drysdale@elec.gla.ac.uk)

Received 26 August 2008

**ABSTRACT:** We present a parallel implementation of the three-dimensional alternating direction implicit finite-difference time-domain (ADI-

*FDTD) method in Cartesian coordinates using the message passing interface (MPI) library. Parallel implementations not only speed up computations but also increase the maximum solvable problem size. The application of the ADI scheme results in freeing the time-step size from the Courant-Friedrichs-Lewy stability constraint. We demonstrate a speedup of the ADI-FDTD method through parallelization, even though the communication overhead between the processors is proportional to the volume of the domain, rather than just the surface area of the sub-domains as for standard parallel FDTD. We benchmarked our code on an IBM p690 symmetric multiprocessor and also a distributed memory computer cluster with a high-bandwidth Infiniband interconnect. In both cases, satisfactory scalability and efficiency was demonstrated for simulation domains comprising up to 8 billion mesh cells. © 2009 Wiley Periodicals, Inc. Microwave Opt Technol Lett 51: 1298–1304, 2009; Published online in Wiley InterScience (www.interscience.wiley.com). DOI 10.1002/mop.24310*

**Key words:** ADI-FDTD method; computational electromagnetics; parallel processing; high-performance computing

## 1. INTRODUCTION

The alternating direction implicit finite-difference time-domain (ADI-FDTD) method [1, 2] provides an efficient approach to the analysis of problems involving objects with fine features relative to the wavelengths of interest. The efficiency results from the unconditional stability of the method at the expense of increased computational burden in comparison to the standard Yee's FDTD [3]. Although a single ADI-FDTD update step usually requires 6–8 times more computation time than a standard FDTD update, the total runtime is less if the mesh is finer than  $\sim 120$  cells per wavelength [4]. Consequently, the ADI-FDTD technique has proven useful for the analysis of integrated circuit interconnects [5] and microstrip and stripline microwave circuits [6].

A parallel ADI-FDTD implementation is required not only to speed up computations but also increase the maximum solvable problem size. To the best of our knowledge, the first implementation of parallel ADI-FDTD used the specialized Cray MTA architecture and results were reported only for small domains of up to 8 million mesh cells [7]. We recently reported preliminary results of an implementation on the more widely available symmetric multiprocessor (SMP) and distributed memory computer cluster (DMCC) architectures, for small domains and in the case of the DMCC, only low bandwidth interconnect [8]. In this article, we present a comprehensive and expanded report on the implementation and performance of parallel ADI-FDTD on these architectures, including for the first time DMCC with high bandwidth interconnect. We describe the implementation, including domain decomposition and data communication scheme in Section 2. We report detailed performance benchmarking for both small and large domains (up to 8 billion mesh cells), comparisons between single and double precision floating point implementations, and Mur 1st-order and CFS-PML boundary conditions in Section 3. We illustrate an application of the code to microstrip antenna analysis in Section 4 and give our conclusions in Section 5.

## 2. PARALLEL ADI-FDTD METHOD

Every ADI-FDTD iteration consists of two substeps, each involving the solution of tridiagonal matrix systems of equations over the  $xy$ ,  $xz$ ,  $yz$  planes of the domain, along the  $z$ ,  $y$ ,  $x$  directions, respectively, to update the electric field components. The complex frequency shifted perfectly matched layer CFS-PML [9] boundary condition is used to reduce reflections at the edges of the domain for simulation of the antenna problems in open space. For the sake of brevity, we derive only the first substep  $E_x$  update formula in a space that has arbitrary complex permittivity that varies as a

function of position but constant permeability ( $\mu = \mu_0$ ,  $\sigma_m = 0$ ). The  $E_x^{n+1/2}$  update equation takes the form:

$$E_x^{n+1/2}|_{i+1/2,j,k} = C_a|_{i+1/2,j,k} E_x^n|_{i+1/2,j,k} + C_b|_{i+1/2,j,k} \times \left[ \frac{H_z^n|_{i+1/2,j+1/2,k} - H_z^n|_{i+1/2,j-1/2,k}}{\kappa_y|_{i+1/2,j,k} \Delta y} - \frac{H_y^{n+1/2}|_{i+1/2,j,k+1/2} - H_y^{n+1/2}|_{i+1/2,j,k-1/2}}{\kappa_z|_{i+1/2,j,k} \Delta z} \right] + \Psi_{exz}^n|_{i+1/2,j,k} - \Psi_{exy}^n|_{i+1/2,j,k} \quad (1)$$

and the  $H_y^{n+1/2}$  update equation takes the form:

$$H_y^{n+1/2}|_{i+1/2,j,k+1/2} = H_y^n|_{i+1/2,j,k+1/2} + D_b \times \left[ \frac{E_z^n|_{i+1,j,k+1/2} - E_z^n|_{i,j,k+1/2}}{\kappa_x|_{i+1/2,j,k+1/2} \Delta x} - \frac{E_x^{n+1/2}|_{i+1/2,j,k+1} - E_x^{n+1/2}|_{i+1/2,j,k}}{\kappa_z|_{i+1/2,j,k+1/2} \Delta z} \right] + \Psi_{hyz}^n|_{i+1/2,j,k+1/2} - \Psi_{hyx}^n|_{i+1/2,j,k+1/2} \quad (2)$$

The terms  $C_a$ ,  $C_b$ , and  $D_b$  denote material coefficients,  $\kappa_i$ , where  $i = x, y, z$ , are the stretched coordinate metric coefficients,  $\Delta i$  is the discretization-step size along the  $i$  direction, the  $\Psi_e$ , and  $\Psi_h$  terms denote convolution terms which are computed using the recursive convolution method [9]. The update formula for  $E_x^{n+1/2}$  is obtained from (1) and (2):

$$\begin{aligned} & - \frac{C_b}{\Delta z \kappa_z}|_{i+1/2,j,k} \frac{1}{\kappa_z}|_{i+1/2,j,k} \frac{D_b}{2 \Delta z} E_x^{n+1/2}|_{i+1/2,j,k-1} \\ & - \frac{C_b}{\Delta z \kappa_z}|_{i+1/2,j,k} \frac{1}{\kappa_z}|_{i+1/2,j,k} \frac{D_b}{2 \Delta z} E_x^{n+1/2}|_{i+1/2,j,k+1} \\ & + \left[ 1 + \frac{C_b}{\Delta z \kappa_z}|_{i+1/2,j,k} \left( \frac{1}{\kappa_z}|_{i+1/2,j,k-1/2} + \frac{1}{\kappa_z}|_{i+1/2,j,k+1/2} \right) \frac{D_b}{2 \Delta z} \right] E_x^{n+1/2}|_{i+1/2,j,k} \\ & = C_a|_{i+1/2,j,k} E_x^n|_{i+1/2,j,k} \\ & + \frac{C_b}{\Delta y \kappa_y}|_{i+1/2,j,k} [H_z^n|_{i+1/2,j+1/2,k} - H_z^n|_{i+1/2,j-1/2,k}] - \frac{C_b}{\Delta z \kappa_z}|_{i+1/2,j,k} [H_y^n|_{i+1/2,j,k+1/2} \\ & - H_y^n|_{i+1/2,j,k-1/2}] \\ & - \frac{C_b}{\Delta z \kappa_z}|_{i+1/2,j,k} \frac{1}{\kappa_x}|_{i+1/2,j,k} \frac{D_b}{2 \Delta x} [E_z^n|_{i+1,j,k+1/2} - E_z^n|_{i,j,k+1/2}] \\ & + \frac{C_b}{\Delta z \kappa_z}|_{i+1/2,j,k} \frac{1}{\kappa_x}|_{i+1/2,j,k} \frac{D_b}{2 \Delta x} [E_z^n|_{i+1,j,k-1/2} - E_z^n|_{i,j,k-1/2}] + [\Psi_{exz}^n|_{i+1/2,j,k} \\ & - \Psi_{exy}^n|_{i+1/2,j,k}] \\ & - \frac{C_b}{\Delta z \kappa_z}|_{i+1/2,j,k} [\Psi_{hyz}^n|_{i+1/2,j,k+1/2} - \Psi_{hyx}^n|_{i+1/2,j,k+1/2} - \Psi_{hyz}^n|_{i+1/2,j,k-1/2} \\ & + \Psi_{hyx}^n|_{i+1/2,j,k-1/2}] \quad (3) \end{aligned}$$

Equation (3) establishes a set of tridiagonal matrix systems of equations along  $z$  direction. The left hand side of (3) represents constant coefficients of the tridiagonal matrix, whereas the right hand side (RHS) represents a function that has to be computed at each substep. The implementation of a convolutional PML [9] inside the ADI-FDTD scheme contributes only six terms to the RHS of (3) and this does not substantially increase the complexity of the parallel ADI-FDTD algorithm.

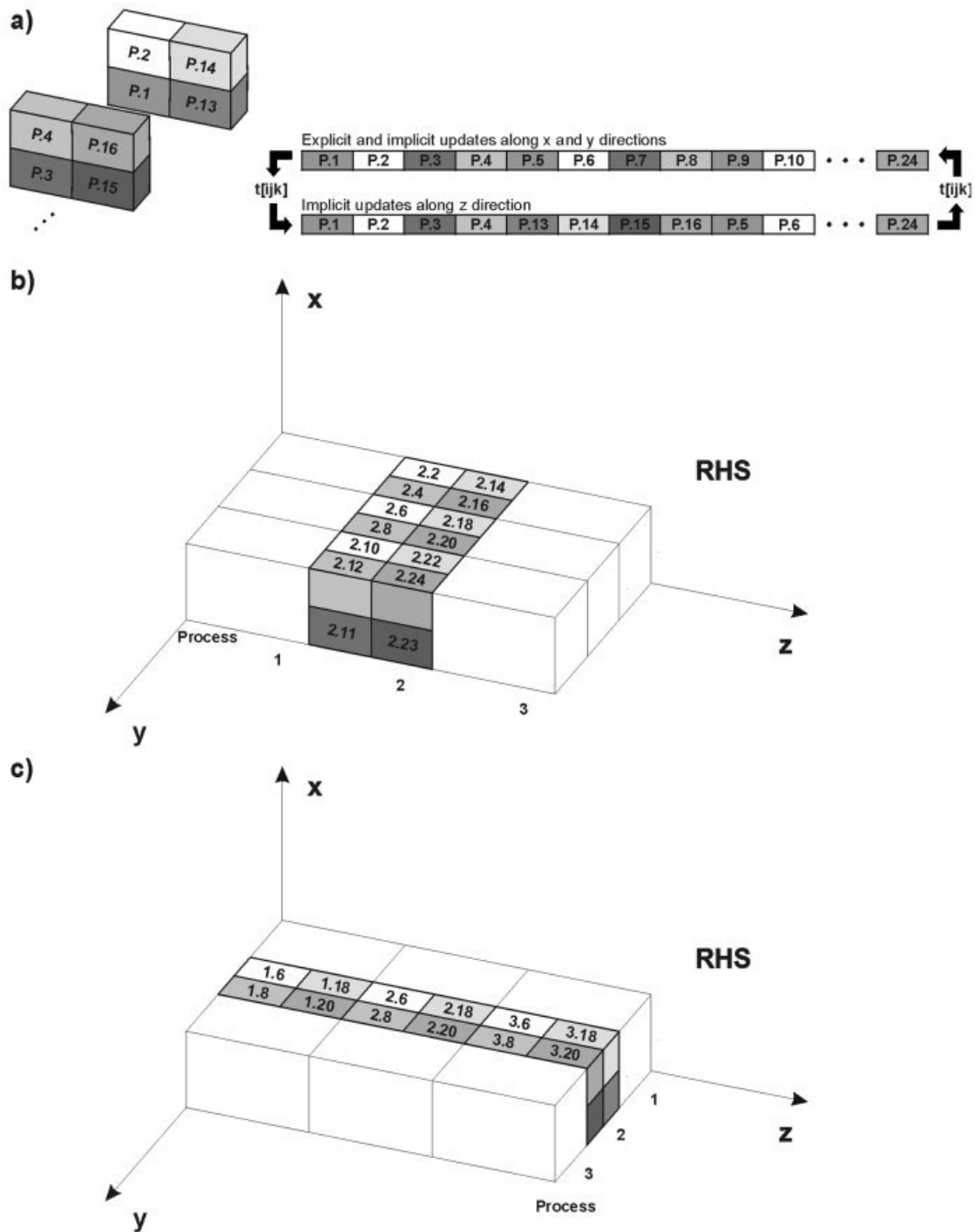


**Figure 1** Diagram of the spatial decomposition scheme for parallel ADI-FDTD scheme. The data order is presented in (a). The highlighted region in (b) (local subdomain) is employed by the 2nd process for all explicit updates and implicit updates of electric field components along  $x$  and  $y$  directions. For implicit update along  $z$  direction RHS data is stored in local domain (b) in an order given by a table  $t[ijk]$  resulting in minimal data handling. RHS data is then assembled into a continuous memory block for input to a tridiagonal matrix system solver as shown in (c). Afterwards, the results are sent back to local subdomains and their ordering (b) is restored based on table  $t[ijk]$

Analogously, all electric field components can be derived for both substeps. The magnetic field is updated explicitly between electric field updates.

To allow the scaling efficiency of the parallel algorithm to be assessed independently of the scaling effect of the CFS-PML, we also implemented electric wall, magnetic wall, periodic, and Mur 1st-order absorbing boundary conditions [10], in addition to CFS-PML. However, we will only present results for Mur

1st-order absorbing boundary condition (ABC) and CFS-PML bounded domains since these are of the most interest.

To speed up computations, the tridiagonal matrices are LU decomposed [11] before the start of the time marching and the respective nonzero diagonals of  $L$  and  $U$  matrices are stored in memory. The tridiagonal matrix system solver data is organized in blocks (vectors) where element  $(i, j, k)$  in the discrete space is related to the element number  $m$  in the vector by:

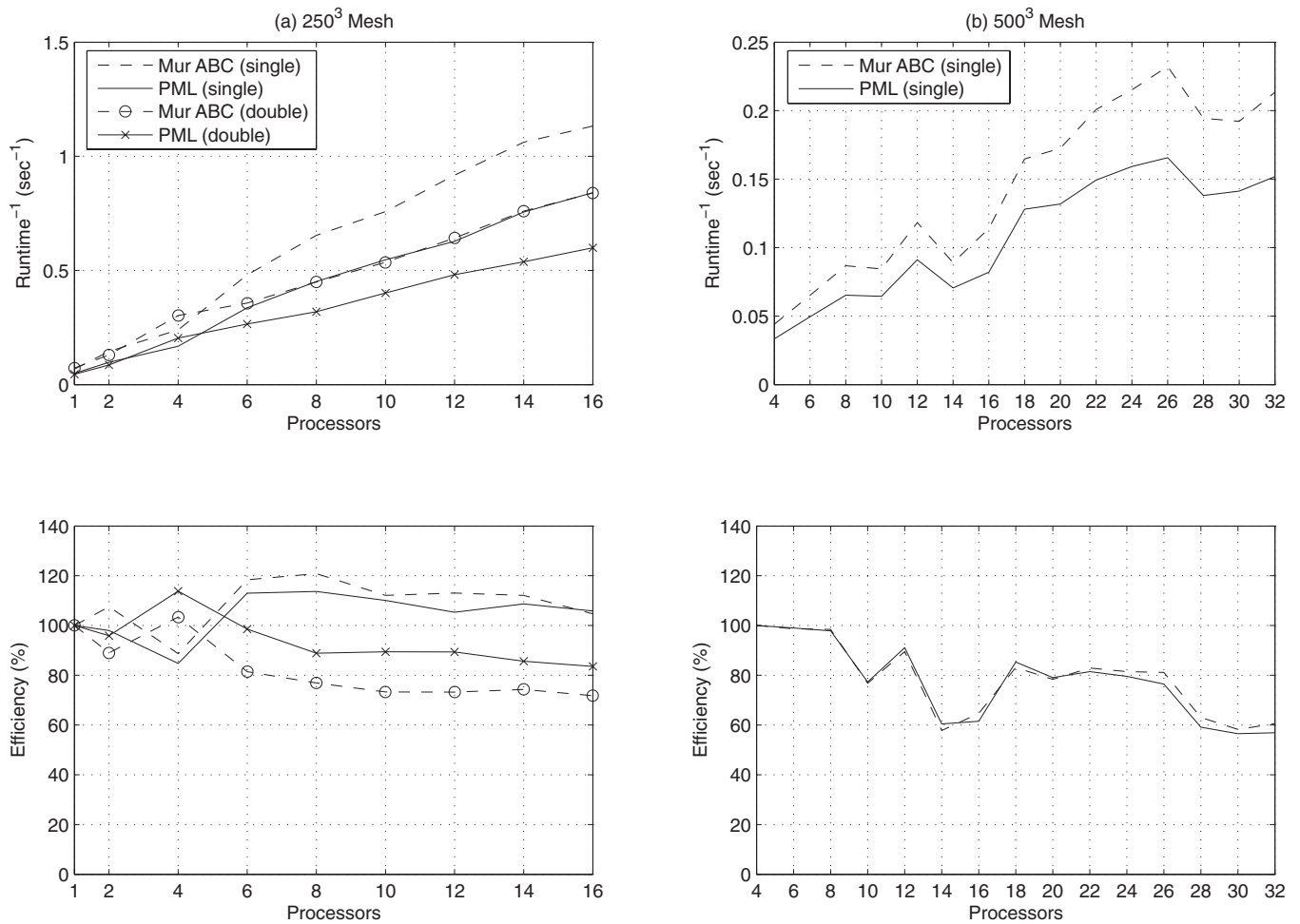


**Figure 2** Reciprocal of the single-step runtime and scaling efficiency for the parallel ADIFDTD method on an IBM p690 shared memory system for (a) 250<sup>3</sup>, (b) 500<sup>3</sup> meshes terminated by Mur 1st-order ABC and PML. In case (a), results are presented for computations performed in single and double numerical precision. Results in (b) were obtained in single precision

$$m = k \cdot \text{size}(x) \cdot \text{size}(y) + j \cdot \text{size}(x) + i, \quad (4)$$

where the operator  $\text{size}(d)$ ,  $d = x, y, z$  represents the side length of the block. Other field components are stored in memory in a similar way.

Each tridiagonal matrix system on each plane is solved by a single processor, with the parallel computer architecture being exploited to solve multiple systems at the same time. This avoids inefficiency associated with using parallelized tridiagonal solvers on small domains. For example, it has been shown that for parallel tridiagonal matrix system solvers, the minimum set of equations for good efficiency is 4000 for a shared memory system and 40,000 for a distributed memory system [12]. Extrapolation of this result to three-dimensional electromagnetics problems indicates that minimum domain side lengths of 4000–40,000 mesh cells would be required before adopting a parallel tridiagonal solver was desirable, but this is currently at or beyond practical memory limits for even large high-performance computers.

The spatial decomposition scheme we developed [8], and expand upon here, subdivides the domain in only two directions ( $y, z$ ). This is well suited to the geometry of VLSI and microwave circuits but does not impose undue constraints on other aspect ratios. For example, we use cubic simulation domains in our benchmarks. We illustrate the decomposition and data-communication scheme with reference to a simplistic example for the sake of clarity. Figure 1

shows a  $6 \times 6 \times 2$  simulation domain that is decomposed for simulation with three processors, with an inset showing the order in which cells are stored in memory in local subdomains according to (4) in Figure 1(a), the arrangement of data for processor two for all explicit updates and the implicit updates of electric field components along the  $x$  and  $y$  directions is shown in Figure 1(b), and the arrangement of the RHS data for processor two during the implicit update along the  $z$ -direction is shown in Figure 1(c). Note that the explicit updates and the implicit updates along the  $x, y$  directions [Fig. 1(b)], are based solely on the local subdomain data so they do not require data stored inside other subdomains. However, they do require the exchange of boundary data at points located on the interfaces between adjacent subdomains as for standard parallel FDTD [4]. For updates along the  $z$  direction, the RHS data from local subdomains is sent to the respective process to assemble the input data block for a tridiagonal matrix solver [highlighted in Fig. 1(c) for processor two]. Therefore, the RHS data is computed in the local domain and stored in memory in an order given by a table  $t[ijk]$  that results in minimal data handling. In other words, the received data is already correctly ordered for direct input to the tridiagonal matrix system solver. After the implicit update of the electric field components along the  $z$  direction, the results are sent back to local subdomains, where the data is restored to its original order by making use of table  $t[ijk]$ . This procedure is repeated in every substep. The larger, volume-pro-

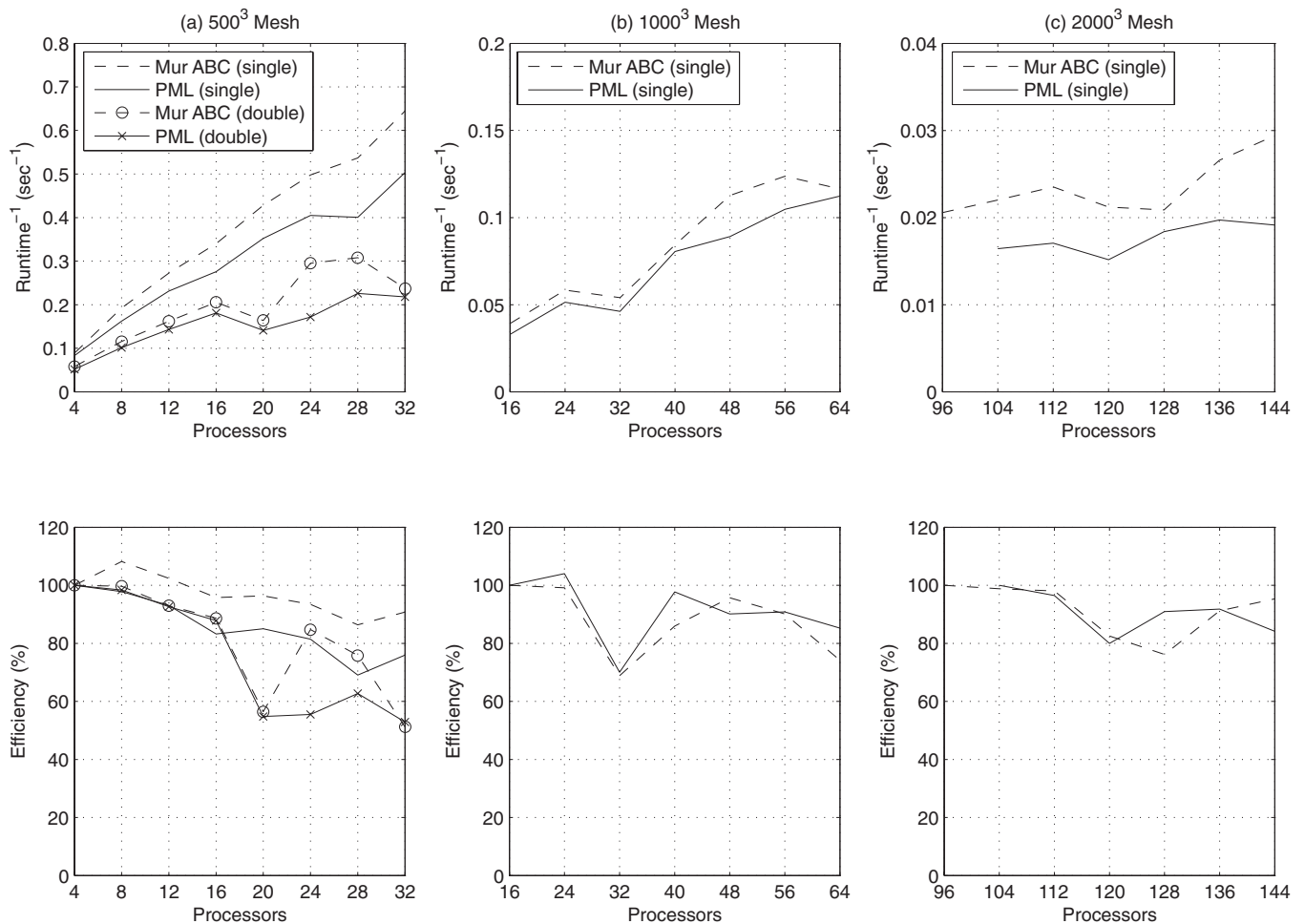


**Figure 3** Reciprocal of the single step runtime and scaling efficiency for the parallel ADIFDTD method on a computer cluster with Infiniband interconnect for (a)  $500^3$ , (b)  $1000^3$ , and (c)  $2000^3$  meshes terminated by Mur 1st-order ABC and PML. In case (a), results are presented for computations performed in single and double numerical precision. In other cases results were obtained in single precision

portional, communication overhead related to updates along the  $z$  direction is the rate limiting step of the method.

### 3. SCALABILITY AND EFFICIENCY

The code was developed in the C programming language using the message passing interface (MPI) library. Simulations were executed on the IBM p690 (Linux, Power 4 + 1.9GHz 32 processors, 32 GB of shared RAM, SMP architecture) and DMCC (36 nodes with two dual-core Opteron 2222 3 GHz processors, 32 GB of RAM per node, DDR *Infiniband* interconnects). We benchmarked the performance using simulation domains of size  $250^3$  and  $500^3$  cells in the case of the IBM p690 and  $500^3$ ,  $1000^3$ , and  $2000^3$  cells in the case of the computer cluster. Computations were performed in single floating numerical precision, however for the smallest domains for each machine we also present results obtained for computations performed in double precision. This allows us to observe the effect of doubling the communication overhead.

For the purpose of benchmarking, the radiation pattern arising from a differentiated Gaussian pulse current point source was calculated. Absorbing boundary conditions must be chosen carefully because these can influence code runtime and scaling efficiency. PML boundary conditions [9] offer reduced reflections compared to Mur 1st-order absorbing boundary conditions [10]. However, the subdomains of a parallel simulation that are truncated by PML regions usually unbalance the distribution of pro-

cessor loads, leading to increased runtime and reduced efficiency. Therefore, we report performance of the developed parallel code with both types of boundaries to allow the scaling performance of the underlying implicit scheme and the impact of choosing PML for reduced boundary reflections to be established.

Runtimes are defined as the duration of a single update step, averaged over large number of the time steps (from 300 to 1200 depending on domain size). The scaling efficiency is defined as in [4]:

$$\text{Efficiency}(k \text{ processors}) = \frac{\text{Runtime}(\text{one processor})}{k \text{ Runtime}(k \text{ processors})} \quad (5)$$

In the case of the larger simulation domains, where data is not available for a single processor simulation, the single processor runtime is estimated based on simulation with the smallest number of processors available under the assumption of linear scalability.

The inverse runtimes and scaling efficiencies for the IBM p690 are presented in Figure 2. For the domain of size  $250^3$  cells we observe an almost linear relation between inverse runtime and number of processors for single precision, which confirms good scalability of the algorithm. Despite having twice the communication overhead, adopting double precision only increased the runtime by 40%. This indicates that the benefit of solving multiple



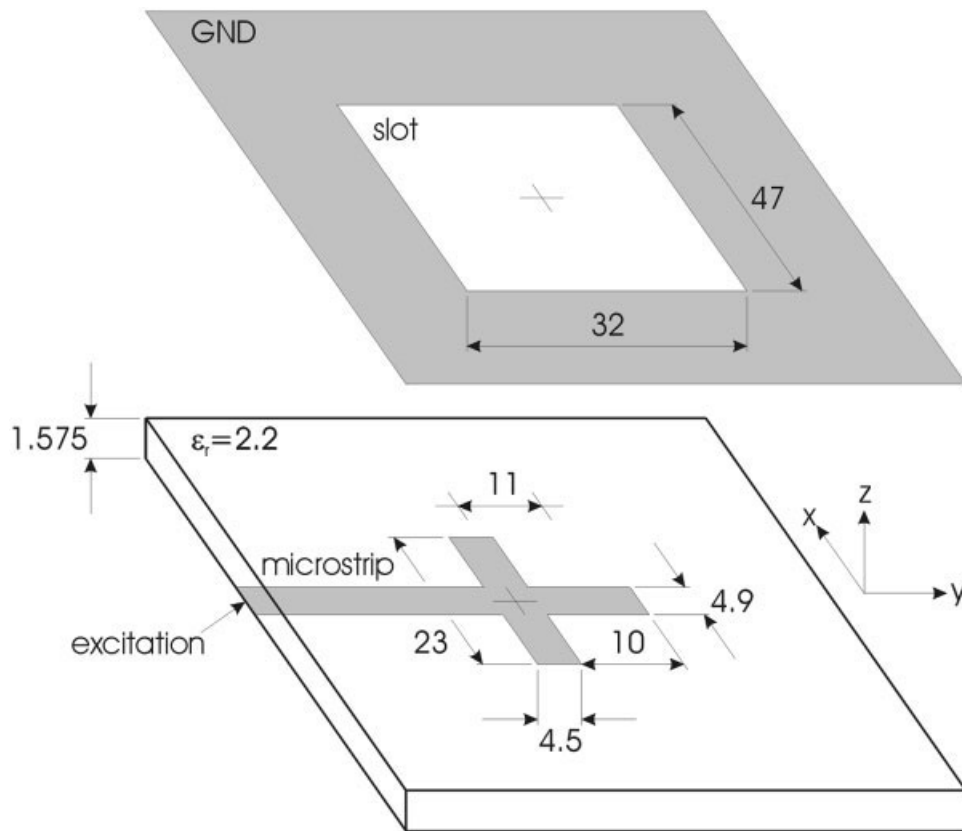


**Figure 4** Diagram of printed slot antenna [13] (all dimensions in millimeters)

tridiagonal matrix systems of equations in parallel outweighs the communication penalty. The efficiency can be slightly above 100% for the smaller domain due to caching effects, i.e., data stored in main memory can fit into the cache when two or more processors are used. Cache effects are more pronounced for single precision computations because more mesh cells can be stored in a given amount of cache memory. For the  $500^3$  domain, although the characteristics suffer from nonlinearities, the computational speedup is significant, with efficiencies above 60%.

The DMCC gave a similar performance improvement from parallelization, as shown in Figure 3. Since the interprocess memory bandwidth is reduced compared to the SMP machine, we observe linear inverse runtime characteristics only for single precision computations in the smallest domain. The double precision runtimes are about twice as long for large number of processors which suggests that communication time outweighs the computation time. Nonetheless, employing parallel ADI-FDTD algorithm for ultra large mesh size computations ( $1000^3$  and  $2000^3$ ) still provides a scalable speedup even for ultra large meshes.

Typically, the extra computational overhead of a PML boundary condition increases the runtime by about 20%, but we do not observe a significant load unbalance when PML is employed. Since Mur and PML characteristics show similar nonlinearities, and the double precision results indicate communication dominates runtime, we conclude that variations in the communication overhead as a function of the number of processors is masking any unbalance in the computational load induced by PML boundary conditions.

#### 4. APPLICATION TO ANTENNA ANALYSIS

To further validate our code and demonstrate its applicability to a design process, we modeled a printed slot antenna, shown in

Figure 4, for which a detailed characterization has already been reported [13]. We simulated far-field antenna characteristics on IBM p690 SMP with use of 8 processors and compared to results from commercially available software (Ansoft HFSS) [14], based on finite element method (FEM). Simulated domain size was equal to  $450 \times 450 \times 135$ . The space discretization step was equal to  $\Delta x = \Delta y = \Delta z = 0.25$  mm, as in the original article [13], which resulted in at least 121 cells per wavelength for the frequencies of interest. Results are presented in Figure 5 for CFL factors (CFL factor =  $\Delta t / \Delta t_{\text{CFL}}$ ) between 1 and 12. As it can be seen, close agreement was obtained between far field patterns. The slight differences in the E-plane pattern are due to a difference in the excitation methods of our ADI-FDTD and the commercial FEM code. This difference between results increases when the CFL factor is increased. We checked that our ADI-FDTD code is only 3.5 times slower than standard parallel FDTD code (for the same number of processors and CFL = 1). Thus, parallel ADI-FDTD with CFL = 12 was 3.4 times faster than parallel FDTD, indicating the speed advantage of the parallel ADI-FDTD method in the simulation of radiation patterns.

#### 5. CONCLUSIONS

We developed a parallel implementation of the ADI-FDTD scheme and benchmarked its performance on both a symmetric multiprocessor machine (IBM p690) and a distributed memory computer cluster using *Infiniband* interconnect. The scaling efficiency is better than 60%, approaching 100% for a small number of processors, and we have demonstrated good performance for domains of sizes up to 8 billion mesh cells. We achieved better than a factor of three speedup over conventional parallel FDTD when analyzing an antenna structures on a fine mesh. These results

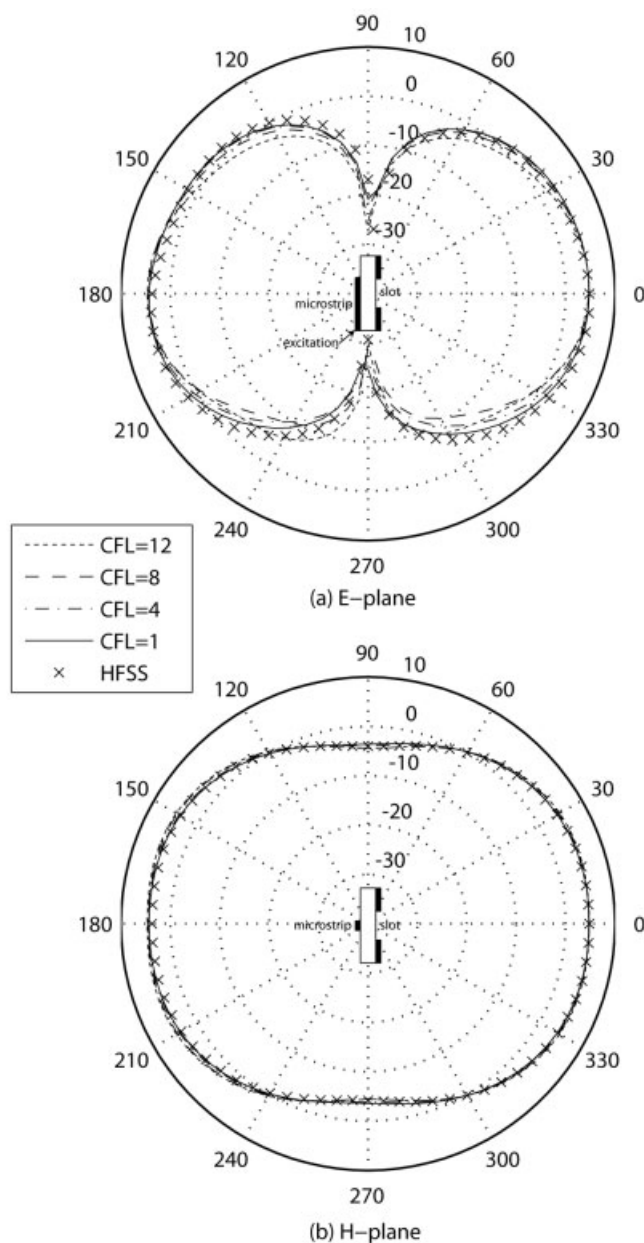


**Figure 5** Radiation patterns in the (a) E-plane (b) H-plane for frequency  $f = 3.3$  GHz as a function of the CFL factor in reference to results from commercial FEM tool (HFSS)

indicate the suitability of parallel ADI-FDTD for analysis of large structures requiring ultrafine meshes relative to the wavelength.

## REFERENCES

1. T. Namiki, 3-D ADI-FDTD method—Unconditionally stable time-domain algorithm for solving full vector Maxwell's equations, *IEEE Trans MTT* 48 (2000), 1743–1748.
2. F. Zheng, Z. Chen, and J. Zhang, A finite-difference time-domain method without Courant stability conditions, *IEEE Microwave Guided Wave Lett* 9 (1999), 441–443.
3. K.S. Yee, Numerical solution of initial boundary value problems involving Maxwell's equations in isotropic media, *IEEE Trans AP* 14 (1966), 302–307.
4. W. Yu, et al., *Parallel finite-difference time-domain method*, 1st ed., Artech House, Boston, 2006, ISBN 1-59693-085-3.
5. I.-J. Choi, et al., ADI-FDTD for the modelling and simulation of VLSI interconnects, *Curr Appl Phys* 5 (2005), 356–364.

6. Y. Yang, et al., Analysis of planar circuits using an unconditionally stable 3D ADI-FDTD method, *Microwave Opt Technol Lett* 46 (2005), 175–179.
7. H. Jordan, et al., Experience with ADI-FDTD techniques on the Cray MTA supercomputer, *Proc SPIE* 4528 (2001), 68–76.
8. T. Stefanski and T.D. Drysdale, Parallel implementation of ADI-FDTD on shared and distributed memory computers, *Proceedings of 2nd EuCAP*, 2007.
9. S.D. Gedney, et al., Perfectly matched layer media with CFS for an unconditionally stable ADI-FDTD method, *IEEE Trans AP* 49 (2001), 1554–1559.
10. G. Mur, Absorbing boundary conditions for the finite-difference approximation of the time-domain electromagnetic-field equations, *IEEE Trans EMC* 23 (1981), 377–382.
11. Z. Fortuna, B. Macukow, and J. Wasowski, *Numerical methods*, 3rd ed., WNT, Warszawa, 1995, ISBN 83-204-1875-5.
12. L. Hluchy, et al., Cluster computation for flood simulations, high-performance computing and networking, Vol. 2110, Springer, Berlin/Heidelberg, 2001, pp. 425–434.
13. Y.-W. Jang, C.-C. Shin, and I.-M. Park, Characteristics of ultrabroad printed slot antenna using FDTD method, *Microwave Opt Technol Lett* 44 (2005), 162–165.
14. Ansoft Corporation, Ansoft HFSS Ver. 11, Ansoft Corporation, Pittsburgh, PA.

© 2009 Wiley Periodicals, Inc.

## NUMERICAL ANALYSIS OF ELECTRICALLY SMALL STRUCTURES EMBEDDED IN A LAYERED MEDIUM

Yongpin P. Chen,<sup>1,2</sup> Jie L. Xiong,<sup>1,3</sup> Weng Cho Chew,<sup>1,3</sup> and Zaiping P. Nie<sup>2</sup>

<sup>1</sup> Department of Electrical and Electronic Engineering, University of Hong Kong, Pokfulam, Hong Kong

<sup>2</sup> School of Electronic Engineering, University of Electronic Science and Technology of China, Chengdu 610054, China; Corresponding author: yongpinchen@gmail.com

<sup>3</sup> Department of Electrical and Computer Engineering, University of Illinois at Urbana-Champaign, Urbana, IL 61801

Received 2 September 2008

**ABSTRACT:** Accurate numerical analysis of electrically small structures embedded in a layered medium is presented in this letter. In our approach, the matrix-friendly layered medium Green's function is implemented for its elegant expression and singularity of lowest order. The current is decomposed into divergence-free part and nondivergence-free part according to quasi-Helmholtz decomposition when frequency tends to zero, to capture both capacitance and inductance physics. Frequency normalization is applied after analyzing frequency scaling properties of different blocks of the matrix system. Similar to the free space case, connection matrix is utilized to make the electro-quasi-static block amenable to iterative solvers. © 2009 Wiley Periodicals, Inc. *Microwave Opt Technol Lett* 51: 1304–1308, 2009; Published online in Wiley InterScience (www.interscience.wiley.com). DOI 10.1002/mop.24302

**Key words:** layered medium; matrix-friendly formulation; low frequency; loop-tree decomposition

## 1. INTRODUCTION

With the development of very large scale integration technology, accurate analysis of electrical components embedded in a layered medium, which are small compared to wavelength yet with complex structures, is in great need. Integral equation method is one of the most favorable methods for layered medium problems. With the help of layered medium Green's function (LMGF) [1–4],